Supporting Information (21 pages, 17 figures, 0 tables):

Ultra-fast, Energy-efficient synthesis of Intermetallics; Microwave-Induced Metal Plasma (*MIMP*) Synthesis of Mg_2Sn

Zhen Fan[1], Mauro Davide Cappelluti[1,2], Duncan H. Gregory[1]*

1. WestCHEM, School of Chemistry, University of Glasgow, Glasgow, G12 8QQ, United Kingdom

2. School of Engineering, University of Glasgow, Glasgow, G12 8QQ, United Kingdom

** Correspondence: Duncan.Gregory@glasgow.ac.uk; Tel.: +44-141-330-6438*

Description of Supporting Information Files

1. Documents

File Name: Supporting Information

Description: Documentation of supplementary experimental and characterisation details.

2. Videos:

File Name: Supporting Video 1

Description: MW synthesis of Mg_2Sn at 200 W for 60 s under a static vacuum ($P < 10^{-6}$ mbar) (*Experiment **8***). The movie is played at 1X speed with a frame rate of 60 f/s.

File Name: Supporting Video 2

Description: MW synthesis of Mg_2Sn at 200 W for 60 s under a dynamic vacuum ($P = 1.2 \times 10^{-1}$ mbar) (*Experiment **5***). The movie is played at 1X speed with a frame rate of 60 f/s.

File Name: Supporting Video 3

Description: MW irradiation of individual Mg powders (30 mg) at 200 W for 60 s under a dynamic vacuum ($P < 10^{-6}$ mbar). The movie is played at 1X speed with a frame rate of 60 f/s.

File Name: Supporting Video 4

Description: MW irradiation of individual Sn powders (60 mg) at 200 W for 60 s under a dynamic vacuum ($P < 10^{-6}$ mbar). The movie is played at 1X speed with a frame rate of 60 f/s.

File Name: Supporting Video 5

Description: MW irradiation of individual SiC powders (100 mg) at 200 W for 60 s under a static vacuum ($P < 10^{-6}$ mbar). The movie is played at 1X speed with a frame rate of 60 f/s.

1. Experimental Details

1.1 Materials synthesis

The Mg/Sn molar ratios, MW irradiation times and reaction atmospheres for all the experiments are detailed in Table 1. The irradiation reactions of experiment **5** and **8** were recorded using a 1080p HD camera with a frame rate of 60 f/s.

1.2 MW irradiation of individual Mg and Sn powders

Either Mg (30 mg) or Sn (60 mg) powder was put into an alumina crucible and sealed in the same quartz tube as described above. The powder was irradiated by MWs with an incident power of 200 W for 1 min under: (i) a dynamic vacuum of $P < 10^{-6}$ mbar; (ii) a static vacuum of $P < 10^{-6}$ mbar; (iii) a dynamic vacuum of $P = 1.2 \times 10^{-1}$ mbar and (iv) a static vacuum of $P = 1.2 \times 10^{-1}$ mbar. A comparison experiment with 100 mg of SiC powder (97.5%, 400 mesh, Sigma-Aldrich) was performed following a similar procedure to the above experiments under a static vacuum of $P < 10^{-6}$ mbar.

Each experiment was recorded using a 1080p HD camera with a frame rate of 60 f/s.

1.3 Materials characterisation

Powder X-ray Diffraction (PXD) was performed using a PANalyticalX'pert Pro MPD diffractometer in Bragg-Brentano geometry with Cu-$K_{\alpha 1}$ radiation ($\lambda = 1.5406$ Å), operating at an accelerating voltage and an emission current of 40 kV and 40 mA, respectively. PXD patterns were collected at room temperature over a range of $15 \leq 2\theta/° \leq 85$ with a step size of either 0.0167113° or 0.0334226° and 55 s per step. PXD data for samples **7** & **19** (Table S1 and Table 1) were collected under anaerobic conditions using a bespoke aluminium sample holder consisting of a sealed chamber with a Mylar window [2]. Rietveld refinements were performed by using GSAS through the EXPGUI interface [3] to calculate the phase fractions of all the obtained samples. Previously published Mg_2Sn, Sn and Mg structures were used as initial model structures for refinement [4, 5]. Typically, the background was modelled using a shifted Chebyschev function (function 1 within GSAS). Zero point, scale factors and cell parameters were refined subsequently in initial cycles. Peak profiles (modelled and adjusted using the Pseudo Voigt function), atomic coordinates and isotropic thermal displacement factors (U_{iso}) were then refined for the main phase (Mg_2Sn). If necessary impurity phases were added following refinement convergence using the main phase. Phase fractions and the peak

profiles, atomic positions and isotropic thermal displacement parameters of any additional phases were refined accordingly. The possibility of non-stoichiometry in the main phase was explored *via* separate refinement of each of the site occupancy factors (SOFs) but values did not deviate significantly from unity and no improvement in the fit was observed. All the SOFs were therefore fixed at 1.0. The refinement profile plots were exported from GSAS and finally processed and plotted.

For the phase-pure sample (Experiment **8**), a PXD pattern collected over 15-120° (2θ) at a step size of 0.0167 ° (150 s / step) was employed for Rietveld refinement using Jana 2006 [6], which permitted a more satisfactory modelling of the peak asymmetry. The refinement procedure was otherwise similar to that implemented with GSAS. The background and profile were modelled by Legendre polynomials and Pseudo Voight functions, respectively. The asymmetry was refined by employing 8 terms of Berar-Baldinozzi correction, which led to an optimised fitting of the profile peaks between the calculated and the observed intensities. Isotropic atom displacement parameters (ADPs) were refined for both Mg and Sn atoms. Attempts were made to refine the SOFs of each metal individually to test for the possible existence of non-stoichiometry. Variation of the SOF for Sn oscillated close to unity without improving the goodness of fit and so the Sn site was fixed as fully occupied. The SOF for Mg consistently refined to a value marginally below 1.0 (but within 3σ of unity) with a slight improvement in the fit. The refinement profile was plotted in the Profile Viewer interface of the software. Visualisation of the crystal structure was fulfilled with the VESTA software package [7].

Scanning Electron Microscopy (SEM) and Energy Dispersive X-ray Spectroscopy (EDX) were performed with a Philips/FEI XL30 ESEM (beam voltage 20 kV, maximum magnification 20 k) equipped with an INCA X-Act detector (Oxford Instruments Analytical, UK). Raman spectroscopy was performed by using a LabRAM HR confocal microscope (Horiba Ltd., Kyoto, Japan) system with a variable optical hole aperture (100 - 300 μm), 600 mm^{-1} grating and a Synapse CCD detector. The excitation source was a Nd:YAG second harmonic laser (Ventus532, Laser Quantum, λ emission = 532 nm, output power 50 mW-1.5W). The spectra were collected over an effective Raman shift range of 50 – 500 cm^{-1}. Thermogravimetric-differential thermal analyses (TG-DTA) were performed using a Netzsch STA 409 PC located in an Ar-fed MBraun glovebox (<0.1 ppm H_2O, <0.1 ppm O_2).

Approximately 15 mg samples of Mg_2Sn from Experiment **8** were heated to 700 °C at a heating rate of 5 °C min^{-1} in an alumina pan under flowing Ar (60 mL min^{-1}).

2. Raman and TG-DTA Analyses

Only one peak was observed in all the Raman spectra of samples synthesised in experiments **8**, **11**, **12**, and **3**, respectively (Figure **S1**). This major peak at 214.5 cm^{-1} corresponds to the longitudinal optical mode band observed in the Raman spectrum of bulk Mg_2Sn sample at 222 cm^{-1} as has been previously reported [8]. No obvious shift in the peak position could be observed in the spectra of the samples investigated.

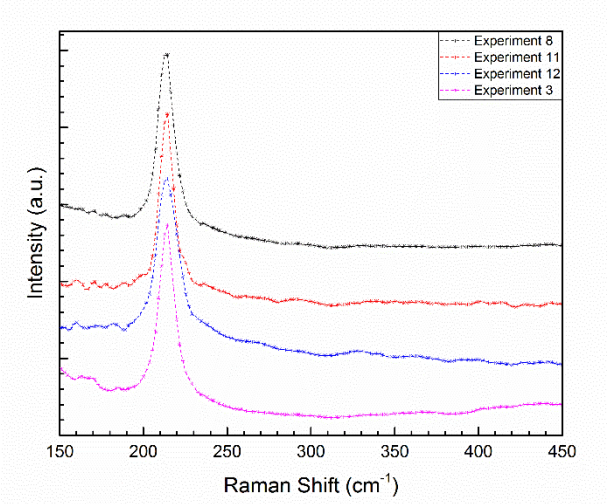

Figure S1. Raman spectra of samples synthesised from experiments **8**, **11**, **12**, and **3**, respectively.

Figure **S2** shows the data from two separate TG-DTA experiments on **8**. Negligible weight changes were observed for both measurements (< 0.37 wt %). For the 1st measurement, the DTA profile is essentially featureless below 650 °C, which marks the onset of a broad endotherm with a maximum at ~675 °C. This maximum is close to the melting point of Mg (650 °C) [9] and PXD data for the post-TG-DTA sample revealed small amounts of MgO and Sn that had not been evident in the diffractograms of **8** (Figure **2** in the manuscript). No endothermic peaks could be found for the 2nd TG-DTA measurement.

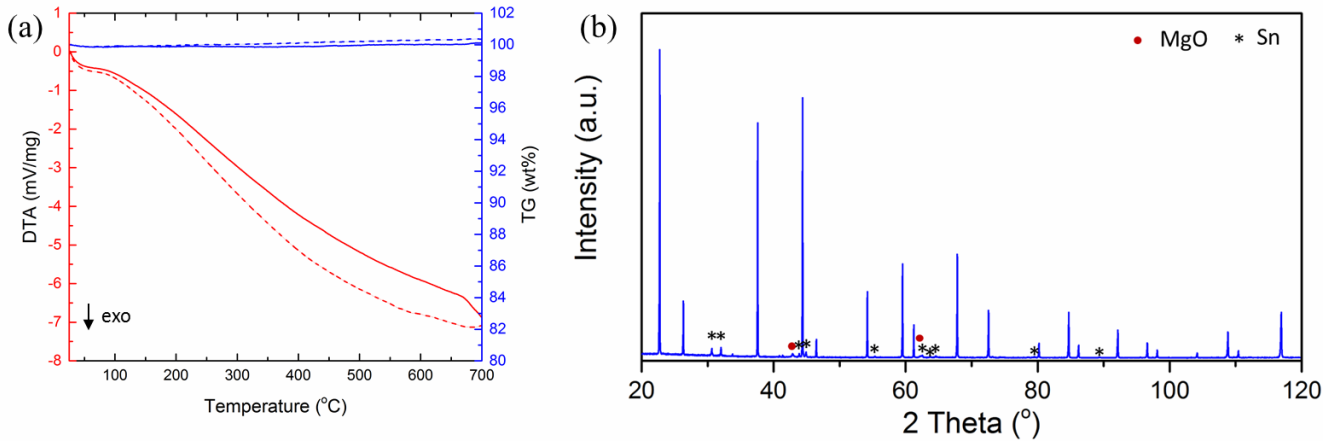

Figure S2. (a) TG-DTA profiles of the sample synthesised in experiment **8**, solid lines:TG-TGA curves of the 1st measurement, dash lines: TG-DTA curves of the 2nd measurement; and (b) PXD pattern of the post TG-DTA measurement sample.

3. MW Irradiation of Individual Mg and Sn Powders

The vapour pressure of Mg/Sn at different temperatures was calculated from the online Vapour Pressure Calculator [10] and plotted. The temperature range was chosen according to the pressure range that our vacuum system could provide. According to Figure **S3**, under a vacuum of $P < 10^{-6}$ mbar such as was used in this study, the Mg could transfer directly from the solid phase to the vapour phase. However, for Sn to transfer to the gas phase under the same vacuum conditions would require a temperature much higher than its melting point (231.93 °C) [9].

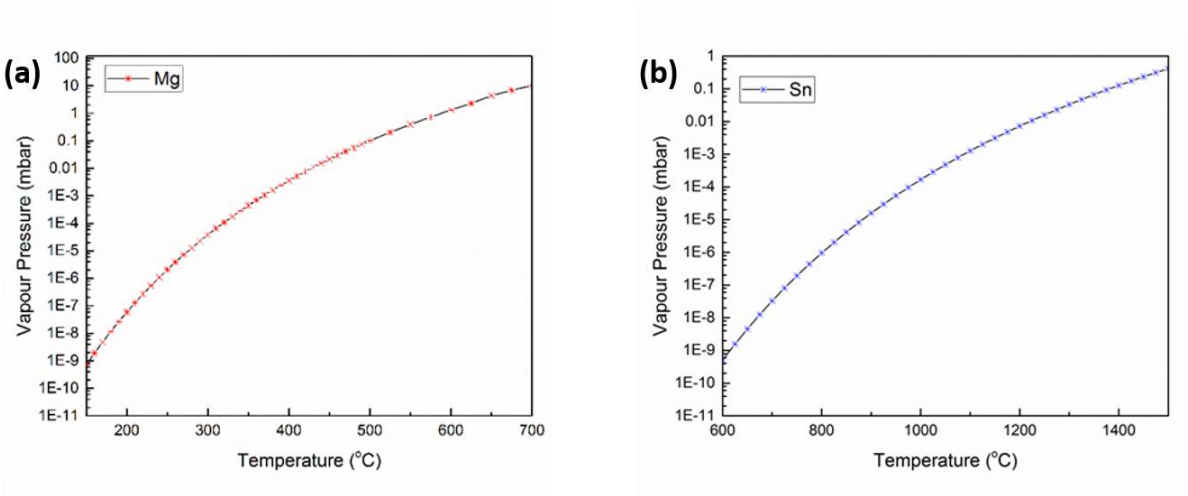

Figure S3. Calculated vapour pressure of (a) Mg and (b) Sn as a function of temperature [10].

3.1 MW Irradiation of Mg powder

Quartz tube (A): Mg plasma was observed under all four different vacuum conditions. The formed Mg plasma interacted with the wall of the quartz tube. The cooled tubes in Figure **S4** clearly show the coating/reaction caused by the Mg plasma.

Alumina crucible (B): As can be seen in Figures **S4a** and **S4c**, effectively no Mg remained in the reaction crucible under dynamic vacuum conditions (of either $P < 10^{-6}$ mbar or $P = 1.2 \times 10^{-6}$ mbar). It can be assumed that vaporisation of Mg and subsequent formation of Mg plasma was promoted by the dynamic vacuum conditions. For the static vacuum conditions shown in Figures **S4b** and **S4d**, both fine powders and pieces of Mg were observed to remain in the reaction crucibles.

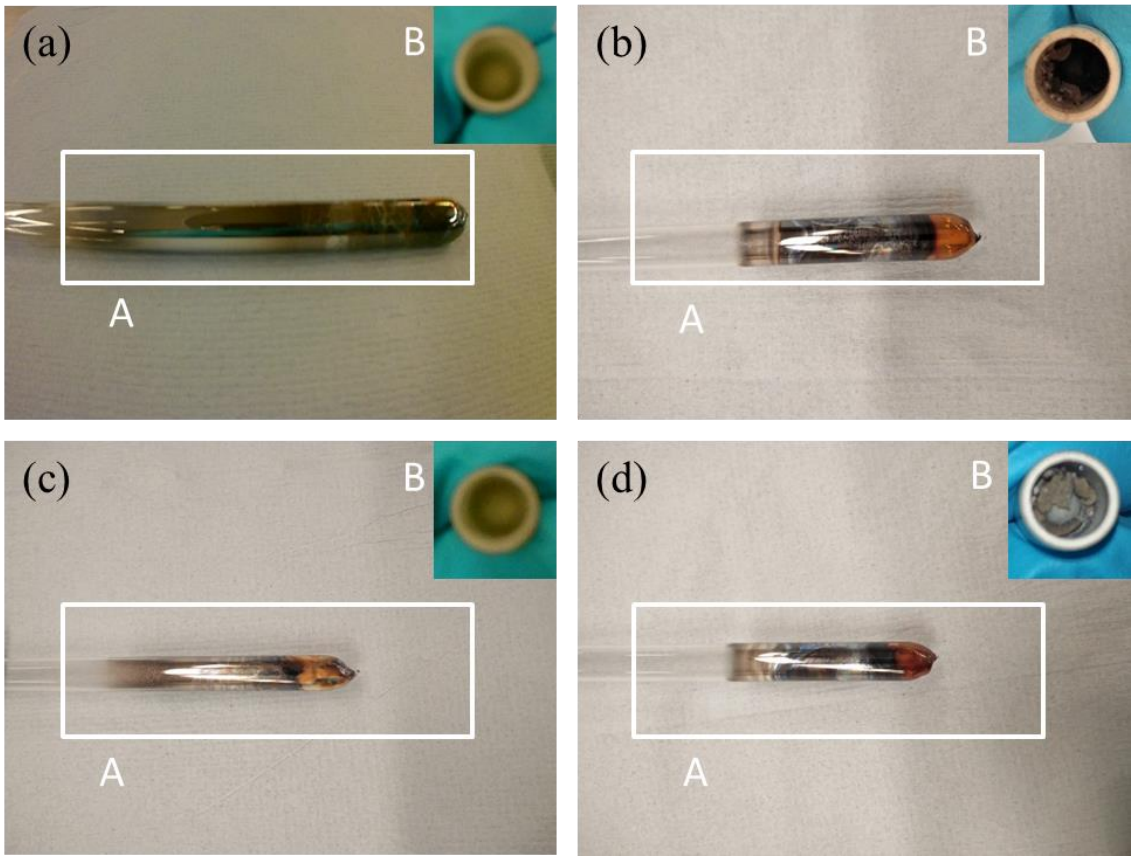

Figure S4. Images of the quartz tube (A) and inner alumina reaction crucible (B; inset) after MW irradiation of Mg metal powder at 200 W for 60 s under different vacuum conditions: (a) dynamic vacuum ($P < 10^{-6}$ mbar); (b) static vacuum ($P < 10^{-6}$ mbar); (c) dynamic vacuum ($P = 1.2 \times 10^{-1}$ mbar) and (d) static vacuum ($P = 1.2 \times 10^{-1}$ mbar).

3.2 MW Irradiation of Sn powder

Quartz tube (A): Plasma formed for all the four different vacuum conditions. Under dynamic vacuum conditions (both conditions of $P < 10^{-6}$ mbar and $P = 1.2 \times 10^{-6}$ mbar; Figures **S5a** and **S5c**), clear deposition of Sn on the wall of the quartz tube could be observed. By comparison, far less deposition of Sn occurred under static vacuum conditions of $P < 10^{-6}$ mbar (Figure **S5b**) and almost negligible deposition of Sn was observed under static vacuum conditions of $P = 1.2 \times 10^{-6}$ mbar (Figure **S5d**). Any deposition is restricted to a localised area directly above the crucible. The extent of Sn deposition contrasts strongly to that of Mg in Figure **S4**, indicative of the different volatility (vapour pressures) of the metals.

Alumina crucible (B): The morphology of the Sn in the reaction crucibles after MW irradiation indicates that melting of Sn occurs and that the Sn droplets aggregate on cooling in all four cases.

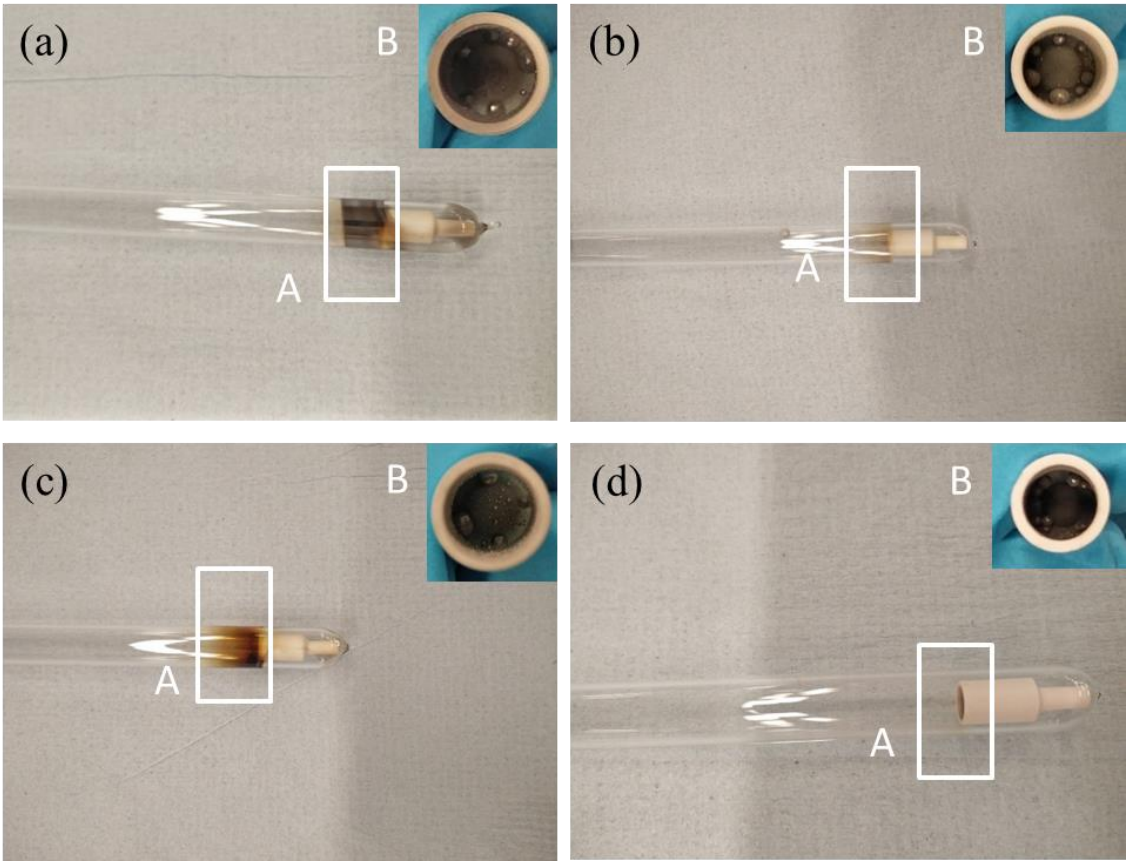

Figure S5. Images of the quartz tube (A) and inner alumina reaction crucible (B; inset) after MW irradiation of Sn powder at 200 W for 60 s under different vacuum conditions: (a) dynamic vacuum of $P < 10^{-6}$ mbar); (b) static vacuum of $P < 10^{-6}$ mbar); (c) dynamic vacuum of $P = 1.2 \times 10^{-1}$ mbar) and (d) static vacuum of $P = 1.2 \times 10^{-1}$ mbar).

3.3 MW Irradiation of SiC powder (A Comparison Experiment)

SiC was chosen as a known high melting point microwave susceptor for control MW irradiation experiments run under identical conditions to **8**. Purple plasma (Supporting Information Video **5**) was generated immediately after the irradiation started, but under the static vacuum conditions it subsided gradually. This plasma and its lifetime is very different from that formed during irradiation of Mg/Sn powders, where the intensity of the plasma is maintained (or even increases) over the MW irradiation duration. Given that a high phase fraction of Mg_2Sn could be obtained in only 5 s under both static and dynamic vacuum conditions ($P < 10^{-6}$ mbar) (Figures **5b** and **7b**), it is reasonable to assume that plasma formation from any residual argon gas has a negligible influence and that it is the interaction between the reactant (Mg, Sn) plasmas that promotes their ultrafast reaction.

4. Rietveld Refinement Profiles for Samples from Experiments Performed under Ar at Atmospheric Pressure

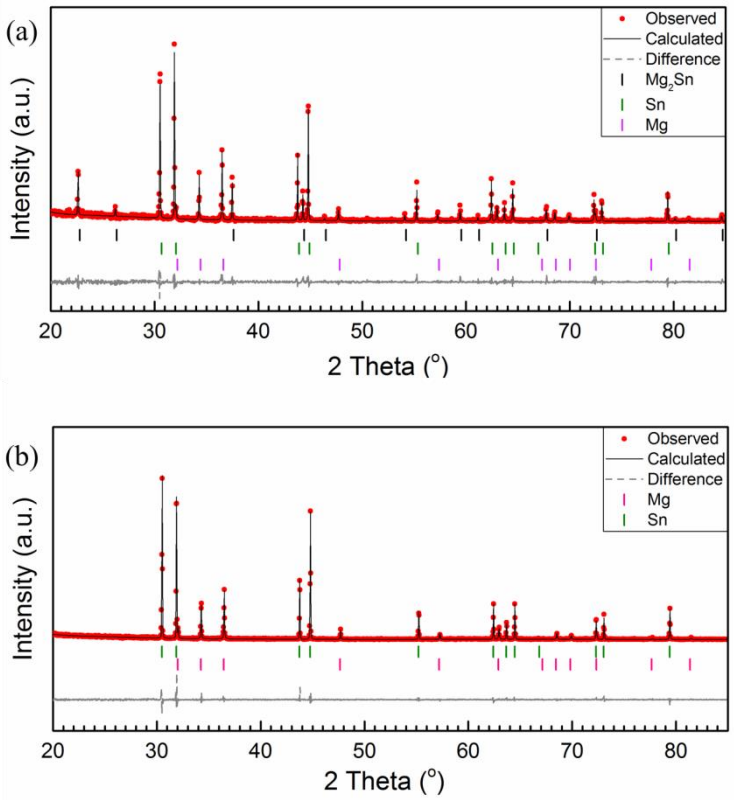

Figure S6. Profile plots from the Rietveld refinements of samples irradiated by MWs with an incident power of 200 W under Ar at atmospheric pressure for: (a) 60 s (Experiment **7**); and (b) 30 s (Experiment **19**), respectively.

5. Rietveld Refinement Profiles, SEM Images and EDX Spectra for Samples from Experiments Performed under a Static Vacuum ($P < 10^{-6}$ mbar)

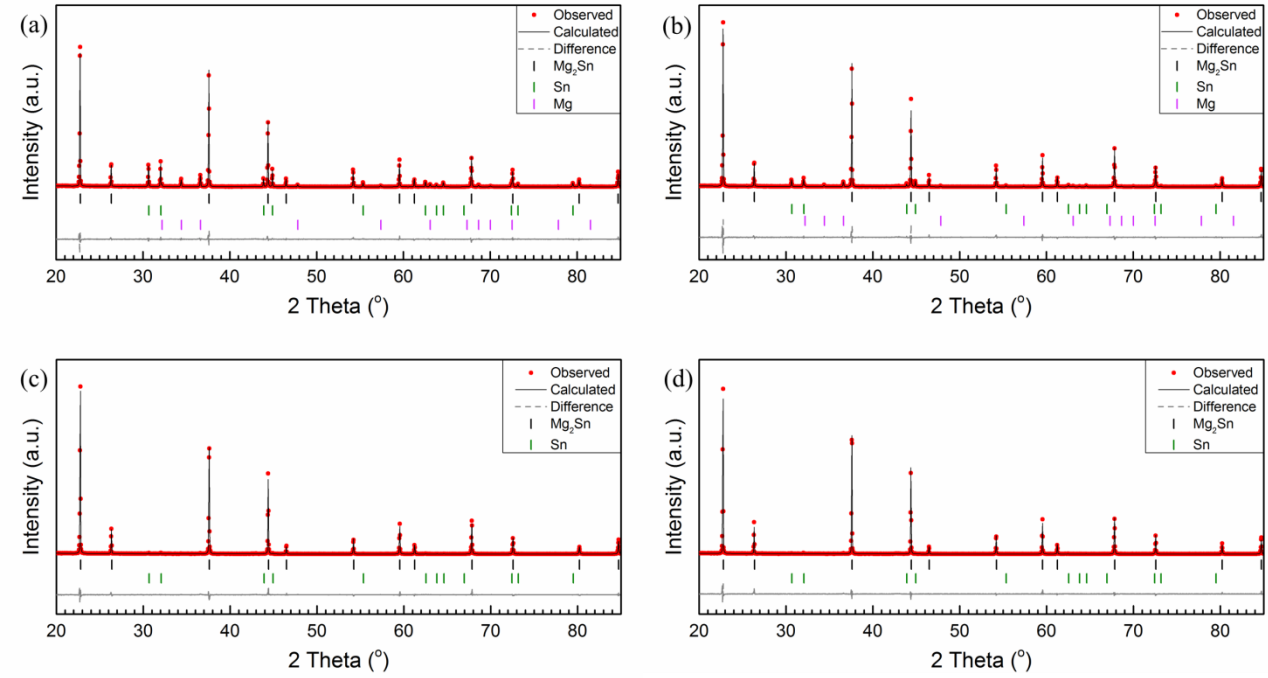

Figure S7. Profile plots from the Rietveld refinements of samples irradiated by MWs with an incident power of 200 W under a static vacuum ($P < 10^{-6}$ mbar) for: (a) 5 s (Experiment **9**); (b) 10 s (Experiment **10**); (c) 30 s (Experiment **11**); and (d) 45 s (Experiment **12**), respectively.

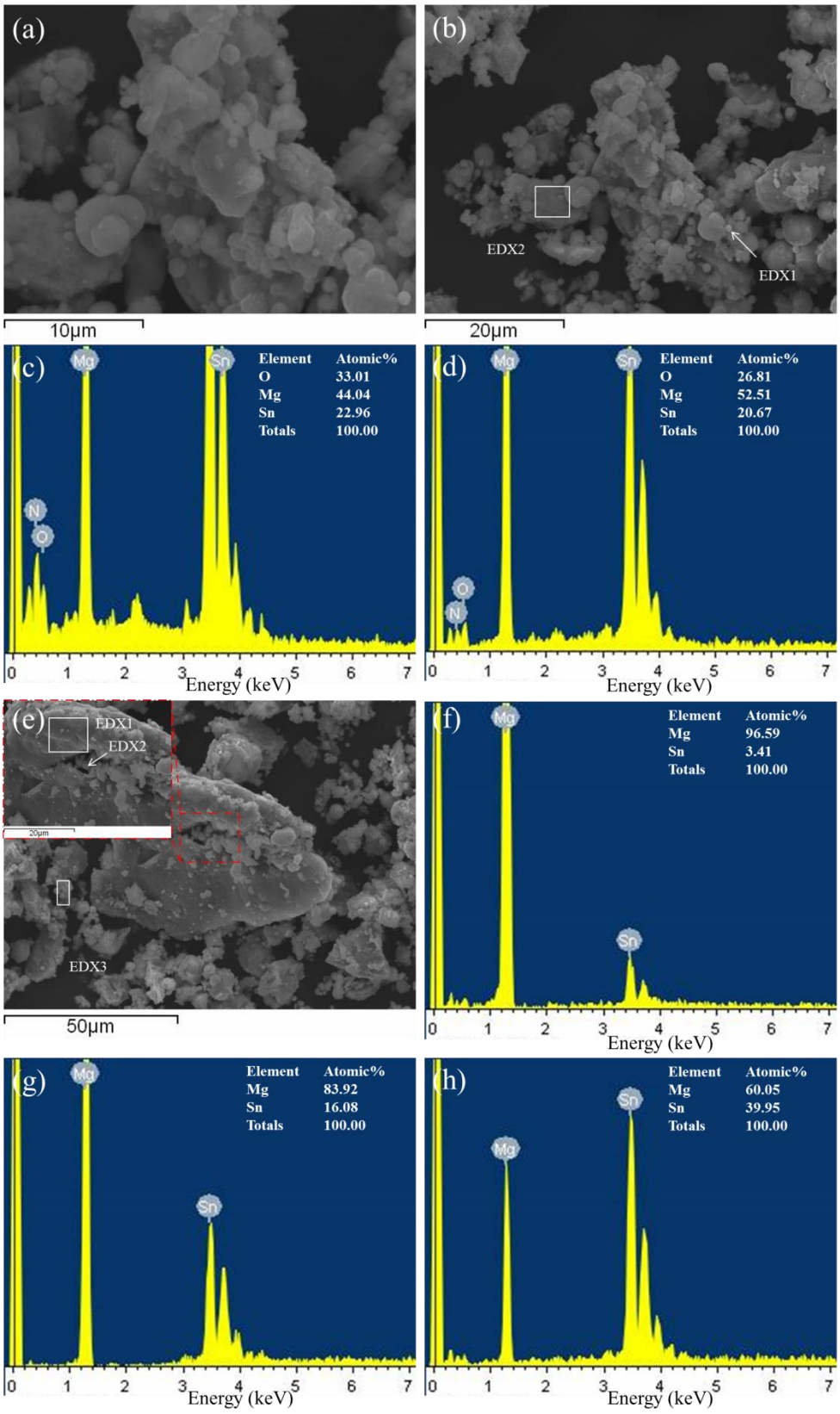

Figure S8 (a, b) SEM images of the fine particles in the products obtained under a static vacuum ($P < 10^{-6}$ mbar) with a MW irradiation time of 5 s; (c, d) EDX spectrum corresponding to EDX1 and EDX2 respectively in (b); (e) SEM image of an unreacted Mg particle among powdered products obtained under a under a static vacuum ($P < 10^{-6}$ mbar) with a MW irradiation time of 5 s and (f - h) EDX spectrum corresponding to EDX1, EDX2, and EDX3 respectively in (e).

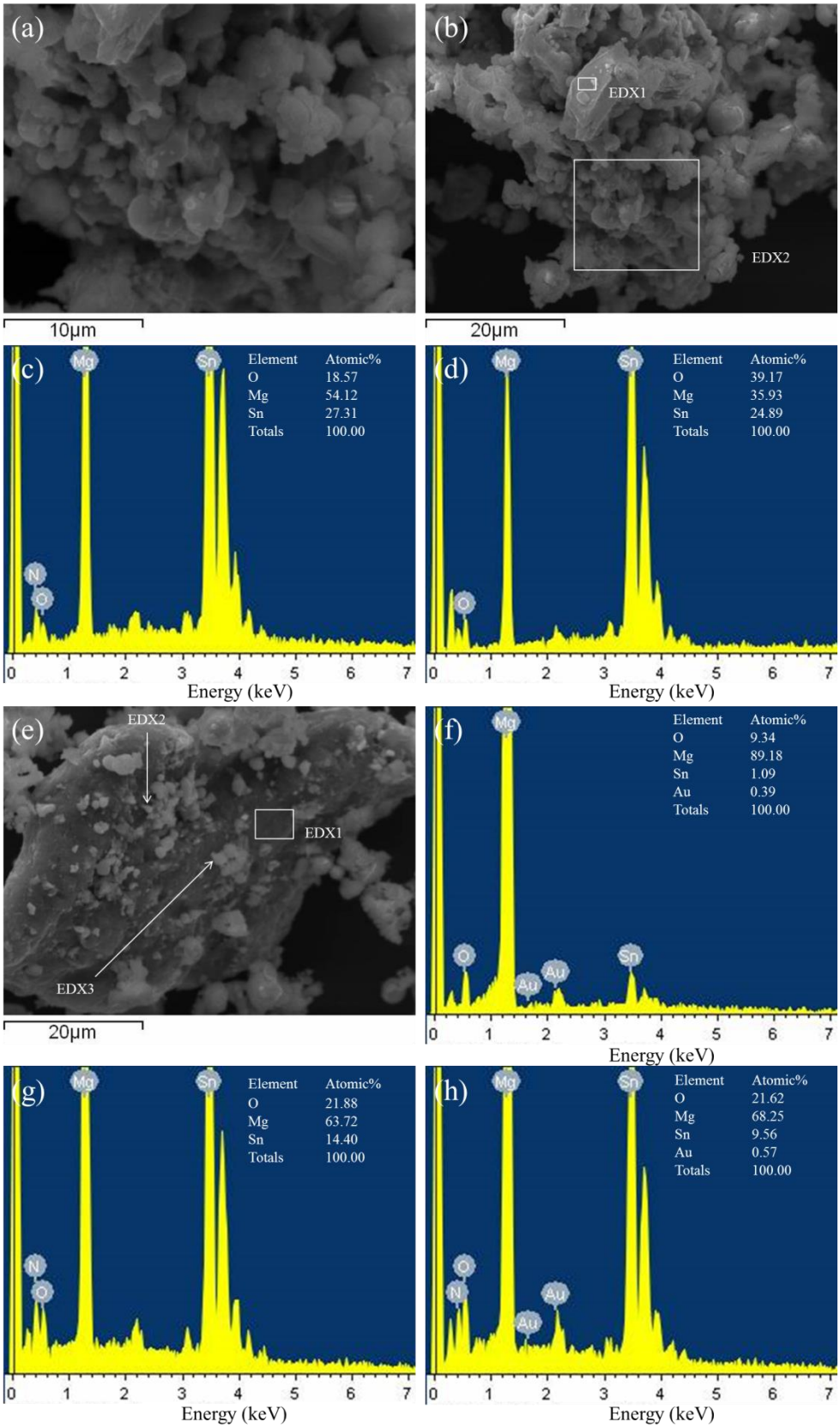

Figure S9 (a, b) SEM images of the fine particles in the products obtained under a static vacuum ($P < 10^{-6}$ mbar) with a MW irradiation time of 10 s; (c, d) EDX spectra corresponding to EDX1 and EDX2 respectively in (b); (e) SEM image of an unreacted Mg particle among powdered products obtained under a under a static vacuum ($P < 10^{-6}$ mbar) with a MW irradiation time of 10 s; and (f - h) EDX spectra corresponding to EDX1, EDX2, and EDX3 respectively in (e).

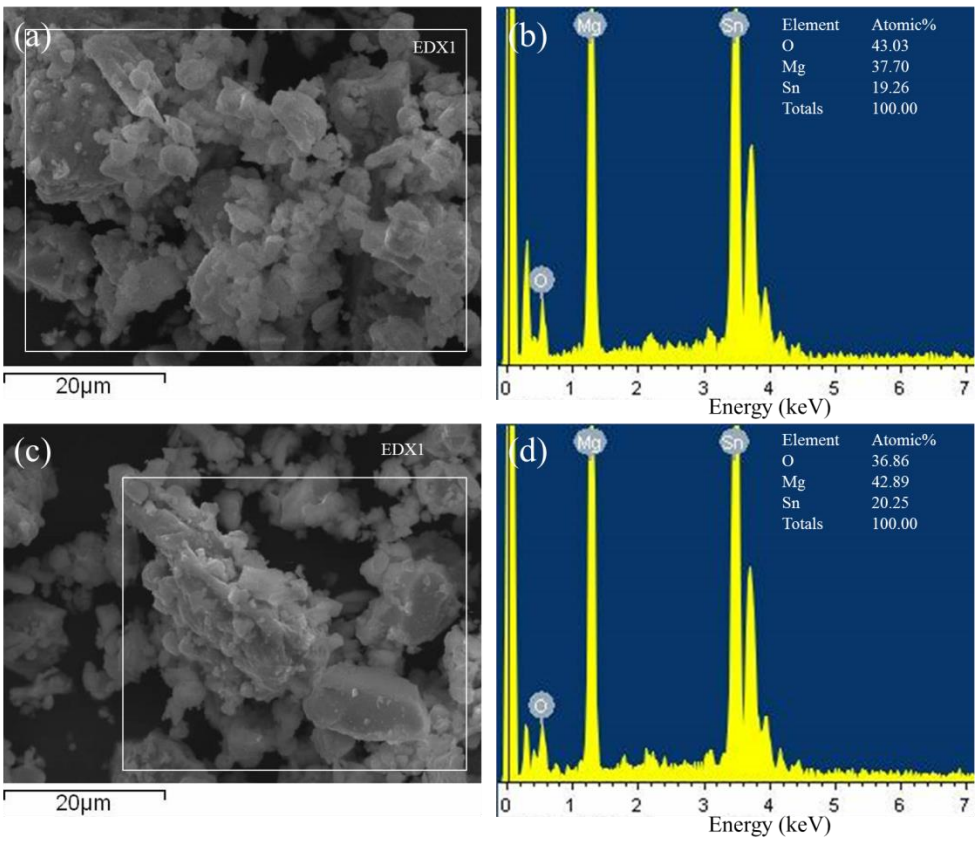

Figure S10 (a, b) SEM image and the corresponding EDX spectrum of the fine particles in the products obtained under a static vacuum ($P < 10^{-6}$ mbar) with a MW irradiation time of 30 s; and (c, d) SEM image and the corresponding EDX spectrum of the fine particles in the products obtained under a static vacuum ($P < 10^{-6}$ mbar) with a MW irradiation time of 45 s.

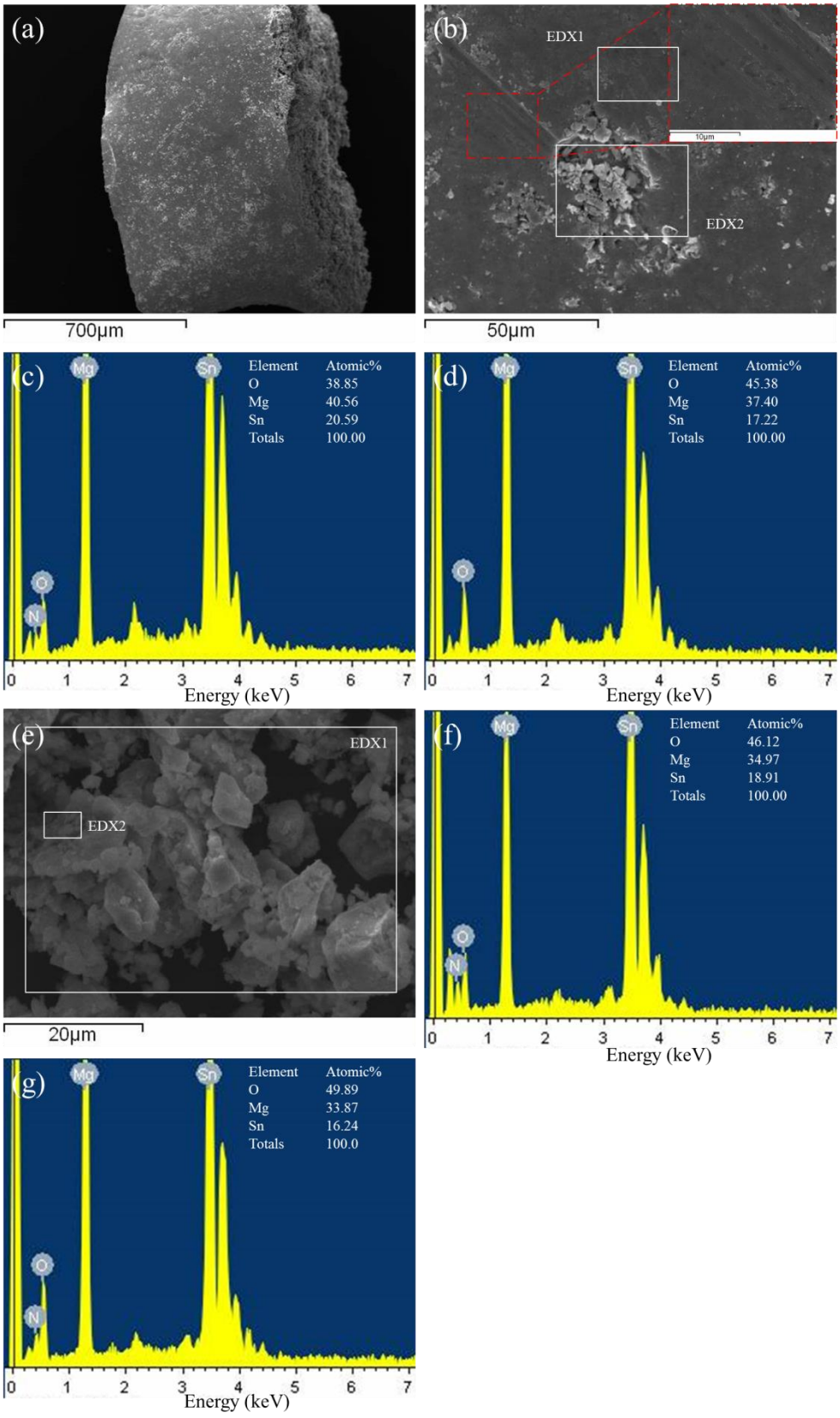

Figure S11 (a, b) SEM images of a condensed piece from experiment **8** synthesised under a static vacuum ($P < 10^{-6}$ mbar) with a MW irradiation time of 60 s; (c, d) EDX spectra corresponding to EDX1 and EDX2 respectively in (b); (e) SEM image of the ground samples from Experiment **8** prepared under a static vacuum ($P < 10^{-6}$ mbar) with a MW irradiation time of 60 s; and (e, f) EDX spectra corresponding to EDX1 and EDX2 respectively in (e).

6. Rietveld Refinement Profiles, SEM Images and EDX Spectra for Experiments Performed under a Dynamic Vacuum (P < 10^{-6} mbar)

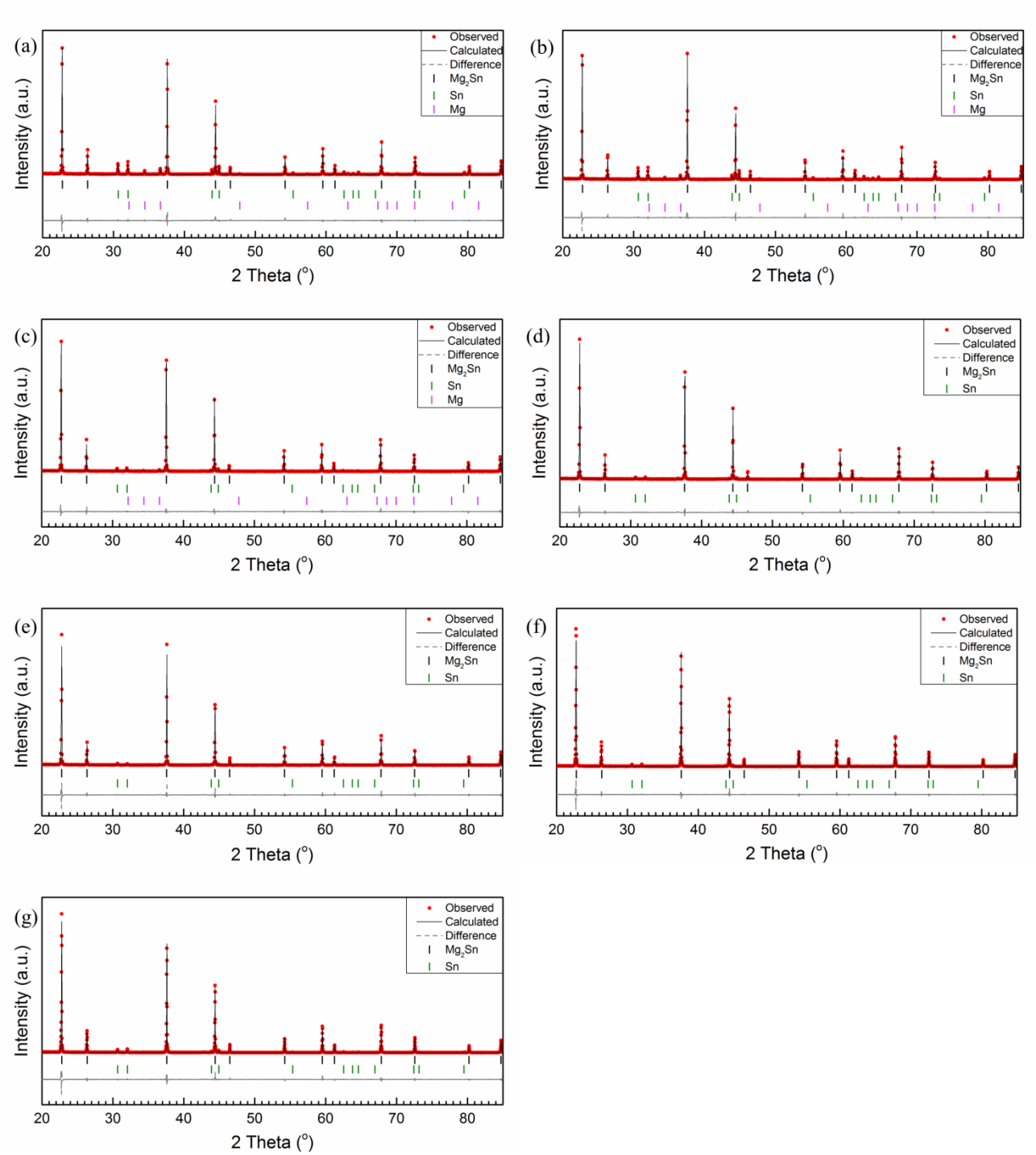

Figure S12. Profile plots from the Rietveld refinement of the samples irradiated by MWs with an incident power of 200 W under a dynamic vacuum (P < 10^{-6} mbar) for: (a) 5 s (Experiment **13**); (b) 10 s (Experiment **14**); (c) 30 s (Experiment **15**); (d) 45 s (Experiment **16**); (e) 60 s (Experiment **3**); (f) 70 s (Experiment **17**); and (g) 80 s (Experiment **18**), respectively.

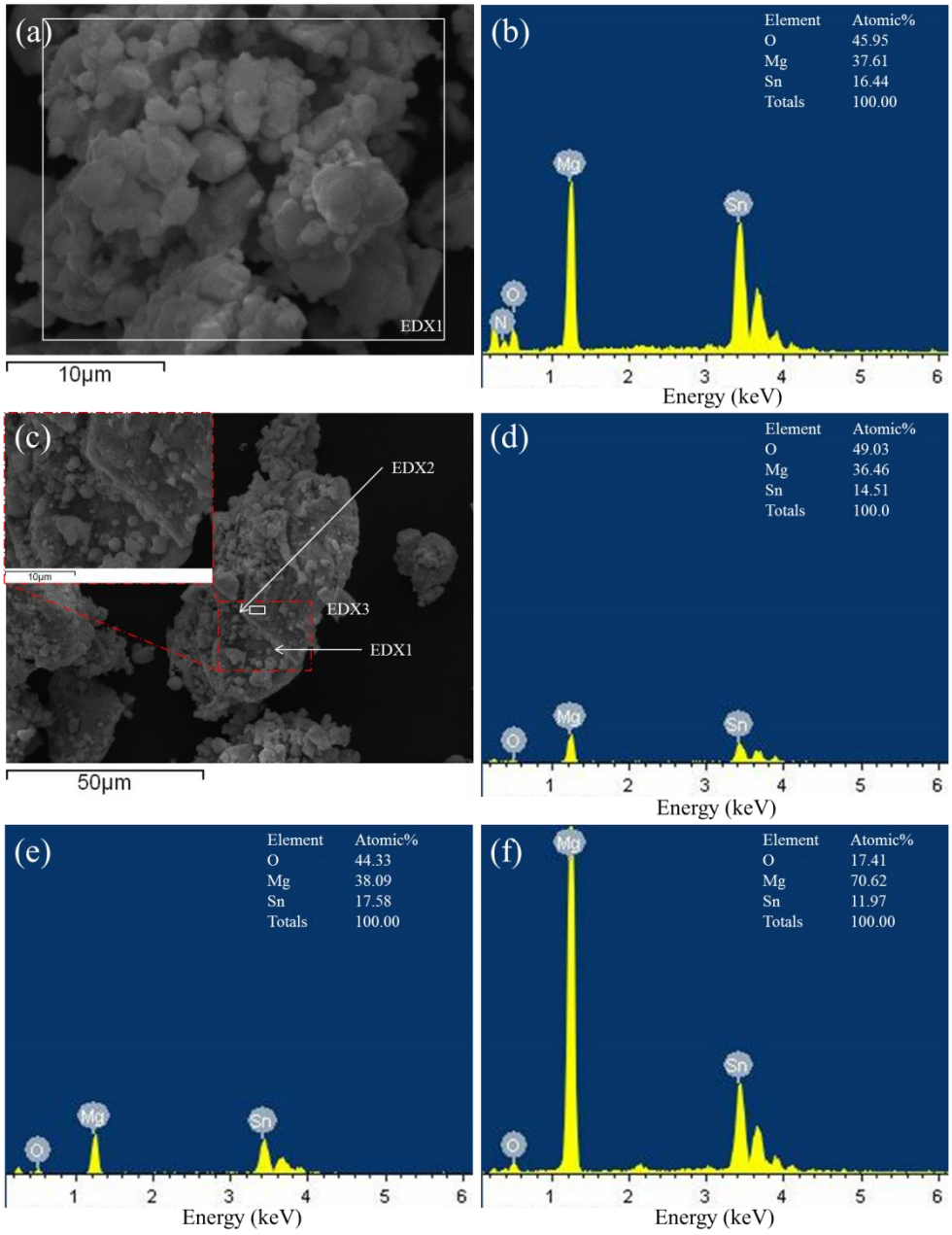

Figure S13 (a, b) SEM image and the corresponding EDX spectrum of the fine particles in the products obtained under a dynamic vacuum ($P < 10^{-6}$ mbar) with a MW irradiation time of 5 s; (c) SEM image of an unreacted Mg particle among powdered products obtained under a dynamic vacuum ($P < 10^{-6}$ mbar) with a MW irradiation time of 5 s; and (d - f) EDX spectra corresponding to EDX1, EDX2, and EDX3 respectively in (c).

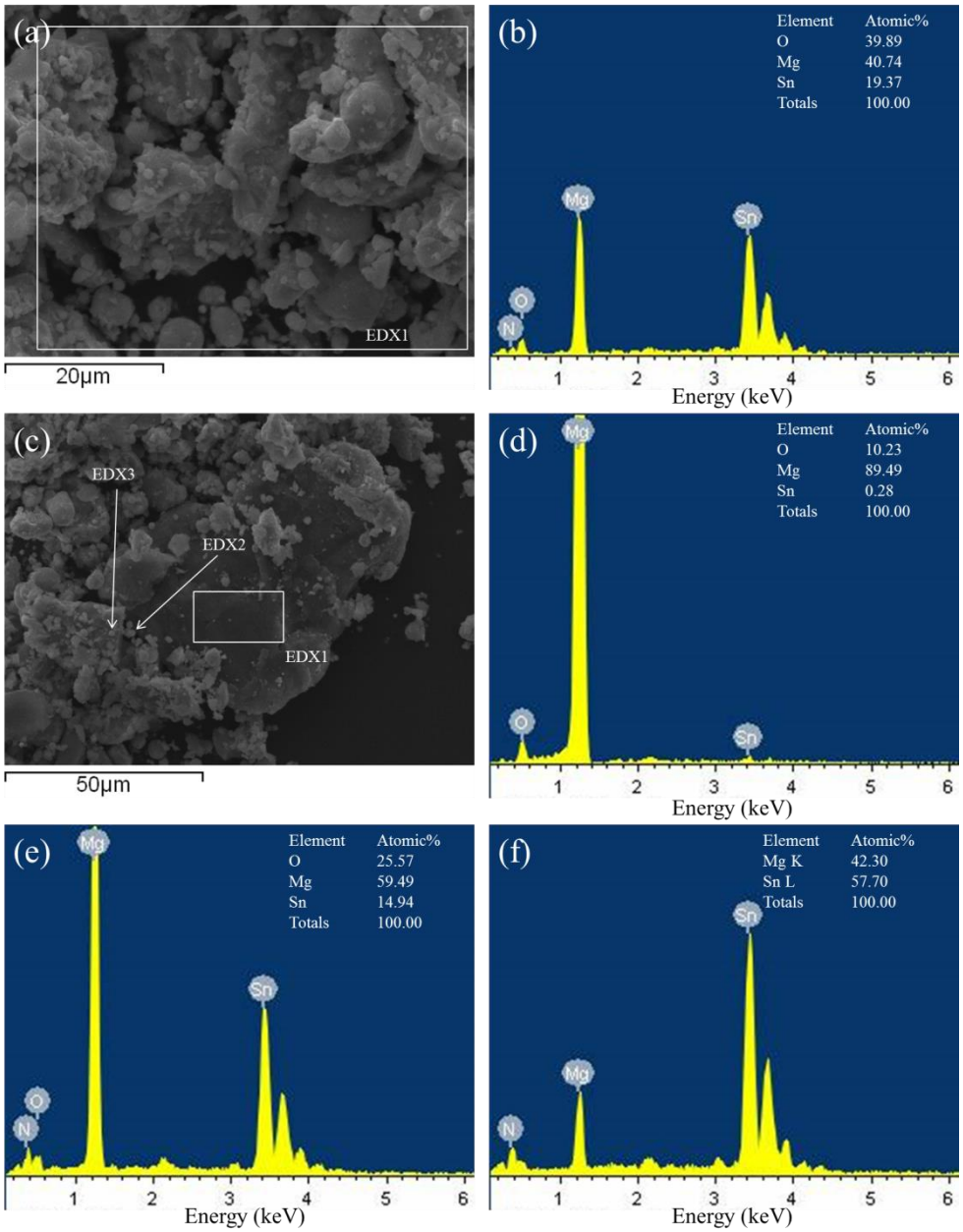

Figure S14 (a, b) SEM image and the corresponding EDX spectrum of the fine particles in the products obtained under a dynamic vacuum ($P < 10^{-6}$ mbar) with a MW irradiation time of 10 s; (c) SEM image of an unreacted Mg particle among powdered products obtained under a dynamic vacuum ($P < 10^{-6}$ mbar) with a MW irradiation time of 10 s; and (d - f) EDX spectra corresponding to EDX1, EDX2, and EDX3 respectively in (c).

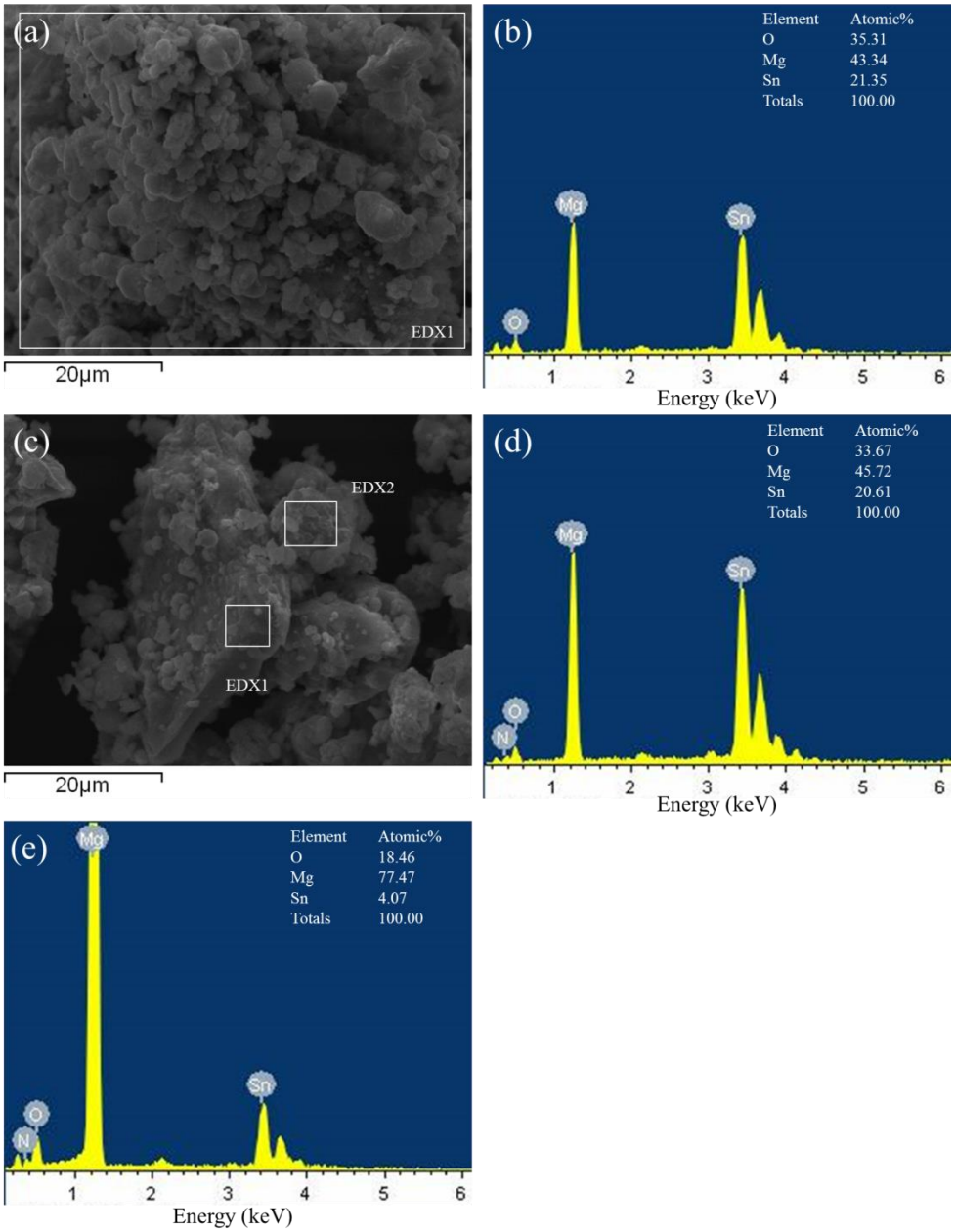

Figure S15 (a, b) SEM image and the corresponding EDX spectrum of the fine particles in the products obtained under a dynamic vacuum ($P < 10^{-6}$ mbar) with a MW irradiation time of 30 s; (c) SEM image of an Mg-rich particle in the products obtained under a dynamic vacuum ($P < 10^{-6}$ mbar) with a MW irradiation time of 30 s; and (d, e) EDX spectra corresponding to EDX1 and EDX2, respectively.

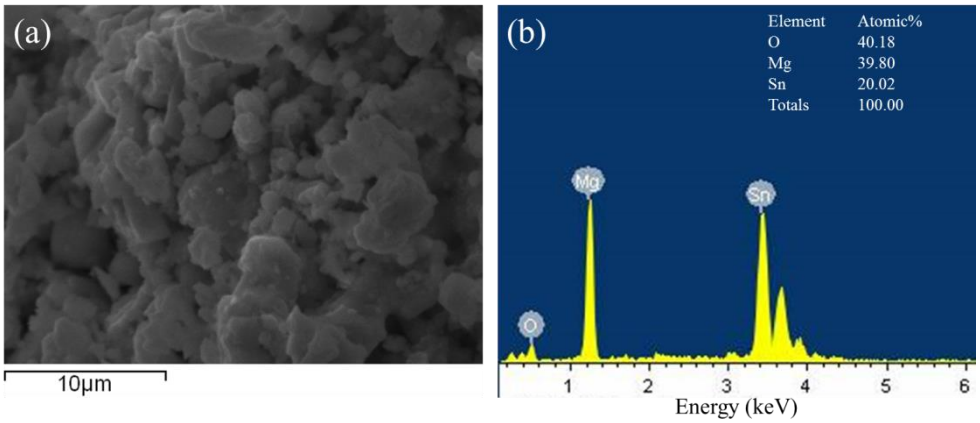

Figure S16 (a, b) SEM image and the corresponding EDX spectrum of the products obtained under a dynamic vacuum (P < 10^{-6} mbar) with a MW irradiation time of 60 s.

7. PXD Pattern of an Experiment Performed with an Mg:Sn Molar Ratio of 2.4:1 under a Static Vacuum ($P < 10^{-6}$ mbar)

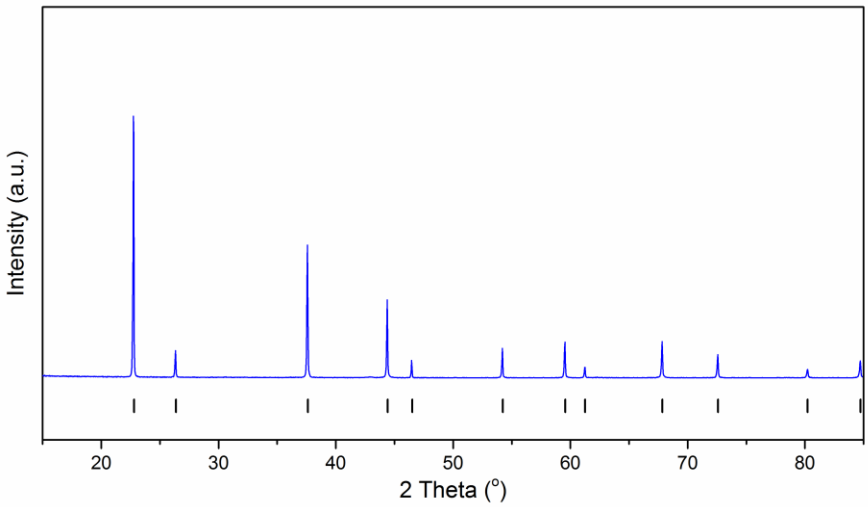

Figure S17. PXD pattern of the sample with an initial Mg/Sn molar ratio of 2.4:1 under a static vacuum ($P < 10^{-6}$ mbar).

Powders of Mg (73 mg) and Sn (148 mg) were ground together and irradiated under a MW incident power of 200 W for 60 s (static vacuum, $P < 10^{-6}$ mbar). All the experimental diffraction peaks (**Fig. S17**) could be indexed to Mg_2Sn. Increasing the Mg:Sn ratio from 2.3:1 (Experiment 8) to 2.4:1 thus has no detectable effect on the purity of the final products, implying additional Mg is lost in the vapour/plasma phase.

References

[1] Robertson, W. D.; Uhlig, H. H. Chemical Properties of the Intermetallic Compounds Mg_2Sn and Mg_2Pb. *J. Electrochem. Soc.* **1949,** 96, 27-42.

[2] Barker, M.G.; Begley, M. J.; Edwards, P. P.; Gregory D. H.; Smith, S. E. Synthesis and Crystal Structures of the New Ternary Nitrides Sr_3CrN_3 and Ba_3CrN_3. *J. Chem. Soc., Dalton Trans.* **1996,** 1-5.

[3] Toby, B. H. EXPGUI, a Graphical User Interface for GSAS. *J. Appl. Cryst.* **2001,** 34(2), 210-213.

[4] Nikitin, E.N.; Tkalenko, E. N.; Zaitsev, V. K.; Zaslavskii, A. I.; Kuznetsov, A. K. A Study of the Phase Diagram for the Mg_2Si-Mg_2Sn System and the Properties of Certain of Its Solid Solutions. *Inorg. Mater.* **1968,** 4, 1656-1659.

[5] Swanson, H. E.; Eleanor, T.; Ruth, K. F. Standard X-ray Diffraction Powder Patterns. *National Bureau of Standards Circular (U. S.).* **1953,** 539, 1-95.

[6] Petricek, V.; Dusek, M.; Palatinus, L. Crystallographic Computing System JANA2006: General features. *Z. Kristallogr.* **2014,** 229(5), 345-352.

[7] Momma, K.; Izumi, F. VESTA 3 for Three-Dimensional Visualization of Crystal, Volumetric and Morphology Data. *J. Appl. Cryst.* **2011,** 44, 1272-1276.

[8] Galkin, N. G.; Galkin, K. N.; Goroshko, D. L.; Chernev, I. M.; Shevlyagin, A. V.; Dozsa, L.; Osvath, Z.; Pecz, B. Non-Doped and Doped Mg Stannide Films on Si(111) Substrates: Formation, Optical, and Electrical Properties. *JPN J. Appl. Phys.* **2015,** 54(7S2), 07JC06.

[9] Hu, F. Synthesis and Characterization of Magnesium-Silicon and Magnesium-Tin Solid Solutions for Thermoelectric Applications. MSc. Dissertation, Texas A&M University, 2012.

[10] Vapor Pressure Calculator. Michael Schmid, IAP/TU Wien Surface Physics Group 2013 – 2018. http://www.iap.tuwien.ac.at/www/surface/vapor_pressure (accessed Sep 30, 2018).